Electronic and magnetic structures that hinder the superconducting state in the collapsed phase of SrCr$_2$As$_2$

U. F. Kaneko [1,*], I. S. S. de Oliveira [2], P. F. Gomes [3], K. R. Tasca [1,†], C. A. Escanhoela Jr.,[1]
N. S. Sangeetha [4,‡] and D. C. Johnston [4]

[1]*Brazilian Synchrotron Light Laboratory (LNLS), Brazilian Center for Research in Energy and Materials (CNPEM),
Campinas, São Paulo, São Paulo 13083-970, Brazil*
[2]*Departamento de Física, Universidade Federal de Lavras, Código Postal 3037, Lavras, Minas Gerais 37200-900, Brazil*
[3]*Applied Complex Network Group of Jataí, Federal University of Jataí, BR 364 km 195, Jataí, Goiás 75801-615, Brazil*
[4]*Ames National Laboratory and Department of Physics and Astronomy, Iowa State University, Ames, Iowa 50011, USA*

The lack of superconductivity in the family of materials AB_2As$_2$ (A = Sr, Ba and B = Cr, Mn) under doping or pressure is an intriguing issue, considering the resemblance of these materials to their cousin materials and superconductors (Ba, Sr)Fe$_2$As$_2$. In this context, the suppression of magnetism together with the presence of electron and hole pockets in the Brillouin zone seem to be fundamental ingredients to explain superconductivity. In this paper, we report a tetragonal to collapsed-tetragonal phase transition in SrCr$_2$As$_2$ under high pressure with the appearance of hole and electron pockets in the Brillouin zone. In this collapsed-tetragonal phase, a residual local magnetic moment in the Cr-ion site and a finite global magnetic energy are derived. This scenario would suggest why superconductivity is prevented in this compound. Our observations were obtained from the analysis of synchrotron x-ray diffraction measurements of polycrystalline samples of SrCr$_2$As$_2$, and using first-principles simulations, under pressures P in the range 1.4 GPa $< P <$ 20 GPa at room temperature.

I. INTRODUCTION

In 2008, iron pnictides generated renewed enthusiasm and activity in the area of non-phonon-mediated superconductor materials [1]. Chemical substitution in the structure AFe$_2$As$_2$ (A = alkali metal, earth alkaline, or rare earth) yields superconductivity when electrons [2–4] and holes [5,6] are placed in the iron and A sites, respectively. The parent compounds also present superconductivity under applied pressures [7–9]; however, hole doping (Cr, Mn) in the iron sites does not trigger superconductivity even under pressure [10,11]. The magnetism is markedly different in these two classes of compounds. Whereas the superconductors suppress a stripe antiferromagnetic order with spins aligned on the ab plane, the (Mn, Cr)-substituted materials present G-type antiferromagnetic order below a high temperature around 600 K with the spins aligned parallel to the c axis. Although charge-nematic fluctuations were required to explain superconductivity [12–16], spin-nematic fluctuations also seem to be an essential ingredient to trigger superconductivity in these compounds [17–23].

A common trend in these systems is the development of a collapsed-tetragonal (cT) phase under pressure. The cT transition occurs well above the optimum T_c dome in EuFe$_2$As$_2$ and BaFe$_2$As$_2$, at pressures of P_{cT} = 8 and 27 GPa, respectively [24,25]. From neutron-diffraction measurements, it was found that CaFe$_2$As$_2$ undergoes an antiferromagnetic orthorhombic to nonmagnetic collapsed-tetragonal phase transition at 0.35 GPa and 50 K, and this structure is unaltered in the superconducting state. Spin fluctuations are not observed in the nonmagnetic cT and nonsuperconducting phase of this compound. At room temperature the cT phase appears between 1.7 and 2 GPa [26–29]. Electrical resistivity and x-ray diffraction (XRD) measurements in KFe$_2$As$_2$ show a T_c increasing from 3.5 to 12 K between ambient pressure and 12 GPa, respectively. Although P_{cT} is around 15 GPa, the upturn in the lattice parameter a occurs in the vicinity of 12 GPa. An interesting change in the dominant carriers was observed in this compound above the superconducting phase at 20 K around P_{cT} [30]. This charge carrier switching and the boost in the superconducting T_c was explained through a Lifshitz transition with minor correlation effects and the development of electron pockets nested to the hole pockets, which might allow for spin fluctuations [31]. Although nesting and spin fluctuations seem to be key ingredients to superconductivity in the pnictides, LiFeAs is a nonmagnetic superconductor material, which presents no nesting and spin fluctuations. Apparently, superconductivity in this compound comes from a Van Hove singularity close to the Fermi level, which is a common fact among the pnictides [32].

A tetragonal to collapsed-tetragonal phase transition was also reported for SrCo$_2$As$_2$ at pressures higher than 6.0 and 6.8 GPa at 7 K and room temperature, respectively,

---

*ulisses.kaneko@lnls.br
†Present address: European X-Ray Free-Electron Laser Facility, Holzkoppel 4, 22869 Schenefeld, Germany.
‡Present address: Institute for Experimental Physics IV, Ruhr University Bochum, 44801 Bochum, Germany.

195114-1

without any sign of superconductivity down to 1.8 K in the tetragonal phase [33]. Recently, XRD in BaCr$_2$As$_2$ presented a tetragonal to cT phase transition at 18.5 GPa and room temperature with no sign of zero resistivity up to 45 GPa down to 1.5 K [34]. In that study, an increase in the density of states suggested that the collapsed phase is electronically driven. Here we investigate the SrCr$_2$As$_2$ compound, which is isostructural to body-centered tetragonal AFe$_2$As$_2$ and, as in Ba(Cr, Mn)$_2$As$_2$, does not present superconductivity [10,11]. We used synchrotron XRD measurements under applied pressure up to 20 GPa, and we also performed a theoretical analysis using density functional theory (DFT) simulations. We observe a collapsed-tetragonal phase occurring at $P_{cT} = 15$ GPa associated with a Fermi surface topology change with possible formation of electron pockets. These observations, added to an increase in the density of states with residual local Cr magnetic moment and global magnetic energy, open space to discuss whether or not superconductivity should appear in SrCr$_2$As$_2$.

II. EXPERIMENTAL AND COMPUTATIONAL DETAILS

A polycrystalline sample of SrCr$_2$As$_2$ was synthesized through solid-state reaction as described in Refs. [35,36]. Synchrotron x-ray diffraction measurements were performed at the XDS beamline of the Brazilian Synchrotron Light Laboratory, Brazilian Center for Research in Energy and Materials (LNLS-CNPEM). An x-ray beam energy of 20 keV ($\lambda = 0.6199$ Å) was selected through the combination of a vertical focusing Rh mirror (VFM), a Si(111) double-crystal monochromator (DCM), and a vertical collimator Rh mirror (VCM), respectively. A beam size of 80×50 μm^2 was focused at the sample position by a Kirkpatrick-Baez (KB) mirror. Diamond-anvil cells with 350-μm culet were used with Re gaskets and Ne gas as the pressure-transmitting medium. A hole of 100 μm diameter was drilled in the center of the gasket indentation, and this chamber was loaded with sample powder with space left in the chamber for Ne gas loading. The luminescence of Chervin ruby balls was used to monitor the pressure inside the chamber. A two-dimensional (2D) Mar-CCD detector was employed to capture the diffraction rings in the transmission geometry, and it was calibrated through the XRD profile of a National Institute of Standards and Technology (NIST) LaB$_6$ powder. All diffraction images of SrCr$_2$As$_2$ as a function of pressure were taken with 600 s of acquisition time. After each pressure increment, scans in the vertical and horizontal directions, perpendicular to the x-ray beam incidence, were performed to guarantee that the beam spot was in the center of the gasket hole.

The simulations were performed based on density functional theory (DFT) as implemented in the QUANTUM ESPRESSO package [37]. The generalized gradient approximation (GGA), in the form proposed by Perdew, Burke, and Ernzerhof [38], was used to describe the exchange-correlation functional. The Kohn-Sham orbitals were expanded in a plane-wave basis set with an energy cutoff of 48 Ry. The electron-ion interactions were taken into account using the projector augmented wave (PAW) method [39]. All geometries were relaxed until atomic forces were lower than 10 meV/Å. The Brillouin zone (BZ) was sampled according
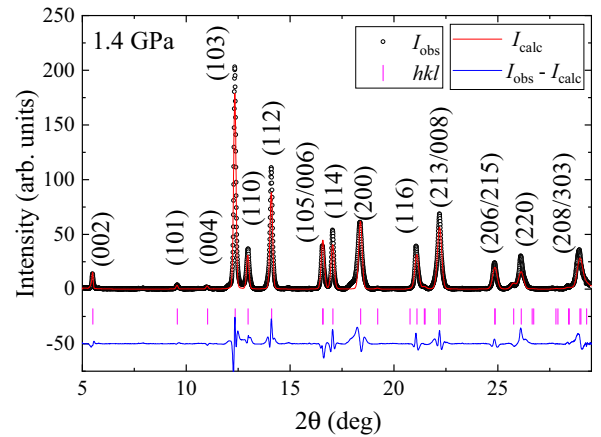
FIG. 1. X-ray diffraction profile of SrCr$_2$As$_2$ (black circles) and its calculated curve (red curve) through a Le Bail analysis at $P = 1.4$ GPa. The difference between the calculated and experimental data is plotted at the bottom as a blue curve. Vertical magenta bars are at the angles calculated for the tetragonal phase with space group $I4/mmm$.

to the Monkhorst-Pack (MP) method [40], using a $12 \times 12 \times 12$ mesh for geometry optimizations. Fermi surfaces were plotted using the FERMISURFER package [41].

III. RESULTS AND ANALYSIS

Figure S1 of the Supplemental Material (SM) [42] shows the 2D diffraction images of four different pressures up to 20 GPa. In addition to the main phase, one phase from the Re gasket, one from solid neon, and a single peak of an unidentified phase were highlighted. In Fig. S2, the intensity as a function of the 2θ diffraction angle was obtained by integrating the diffraction rings along the azimuth angle between 0 and 2π rad for all diffraction images up to 20 GPa. The integrated diffractogram at 1.4 GPa, together with the calculated profile, the 2θ positions of the tetragonal-phase reflections with $I4/mmm$ space group, the difference between the measured and calculated profiles, and the hkl index of each peak as obtained from Le Bail refinement, are presented in Fig. 1. The lattice parameters a and c, the ratio c/a, and volume V as a function of pressure were obtained through a Le Bail refinement and are presented in Figs. 2(a)–2(d). The Le Bail fitting curve, observed profiles, their subtraction, and the expected phases of SrCr$_2$As$_2$ and secondary phases for four selected pressures are shown in Fig. S3. Such a procedure was adopted due to the diffraction profile quality, which in this case was affected by the presence of secondary phases of the Re gasket and Ne pressure-transmitting medium. Additionally, other factors such as low grain size distribution, nonperfect hydrostaticity (see Fig. S4), and preferential orientations under pressure can also affect the quality of the diffraction profile.

It is clearly observed from Figs. 2(a)–2(d) that an upturn in the a parameter, a discontinuity in the c parameter, a slope change in the ratio c/a, and finally a change of 6% of the unit-cell volume as a function of pressure occur around the same pressure of 15 GPa. These features are signatures of a tetragonal (T) to collapsed-tetragonal (cT) phase transition, as observed in similar compounds [29,34], and determine the
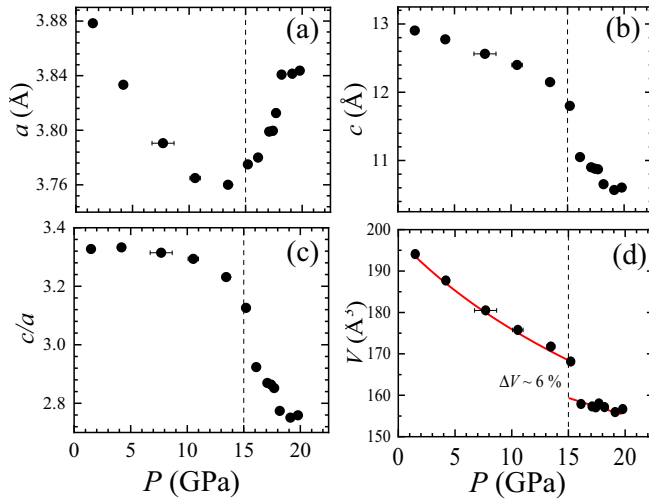
FIG. 2. Results from Le Bail fittings for the lattice parameters (a) a, (b) c, (c) c/a, and (d) unit-cell volume V as a function of pressure P. Solid curves are fits of the volume to the second-order Birch-Murnaghan equation of state before and after the cT transition [43]. Dashed vertical lines mark the transition pressure $P_{cT} = 15$ GPa. Errors smaller than the point sizes are not visible in the plots.

critical pressure as $P_{cT} = 15$ GPa for $SrCr_2As_2$. A second-order Birch-Murnaghan (BM) equation [43], as presented in Eq. (1) in the SM, was employed as the fitting curve of the pressure-volume data in the T and cT phases. The bulk moduli (68 ± 3) and (124 ± 83) GPa and initial unit-cell volume V_0 parameters (198 ± 1) and (176 ± 11) $Å^3$ were obtained from the fitting for the T and cT phases, respectively. In general, there is a bulk modulus stiffening in compounds with similar structure to $SrCr_2As_2$ between the T and cT phases. Such hardening in B_0 is captured by our data analysis, and the bulk modulus values in both phases are within the intervals reported before for similar compounds [25,34,44,45].

Next, we performed DFT simulations for the $SrCr_2As_2$ structure represented in Fig. 3(a). The relaxed equilibrium atomic positions result in the following values for the lattice
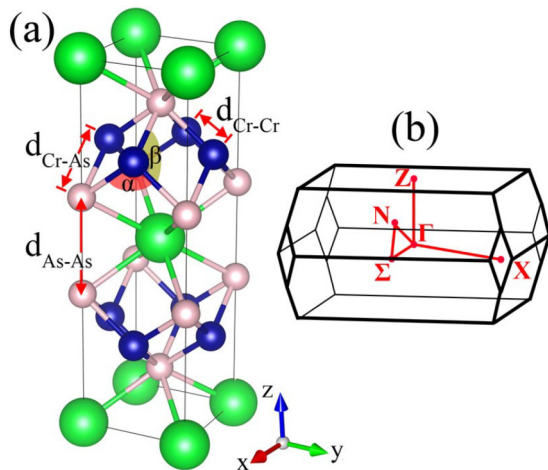
FIG. 3. (a) Body-centered tetragonal $SrCr_2As_2$ crystal structure and (b) its primitive-cell Brillouin zone.
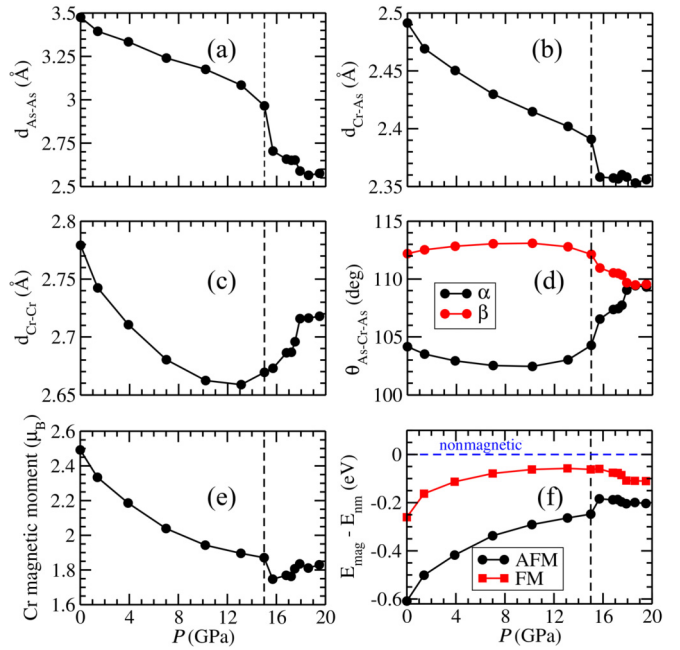
FIG. 4. Interatomic (a) $d_{As–As}$, (b) $d_{Cr–As}$, and (c) $d_{Cr–Cr}$ distances, (d) α and β angles, (e) magnetic moment per Cr atom, and (f) magnetic phase energy as a function of the applied pressure. The vertical dashed lines represent the structural transition pressure P_{cT}.

parameters: $a = b = 3.93$ Å and $c = 13.08$ Å, with a small difference of $\sim 1\%$ from experimental measurements [35]. The effect of the applied pressure is simulated by using the lattice parameters obtained from Le Bail refinement. Thus the unit-cell dimensions are fixed for each pressure value, and the atomic positions are further relaxed. The interatomic As–As, Cr–As, Cr–Cr distances and As–Cr–As angles α and β as a function of pressure from DFT simulations are shown in Figs. 4(a)–4(d). The As–As distance decreases monotonically with increasing pressure up to P_{cT}. Above this pressure, there is a larger drop in $d_{As–As}$; however, the compression rate is virtually the same as before the transition. In agreement with other pnictides, a distance of approximately 3 Å is achieved at P_{cT}, which may be used as a parameter to define the structural transition [46]. From the room-temperature parameters to the maximum applied compression, $d_{As–As}$ decreases by approximately 24%, reaching atomic separation distances of ~ 2.5 Å. This distance approaches the As–As covalent bond distance of ~ 2.4 Å, which is an indication that interlayer As–As bonds begin to develop in the system [34]. This indicates the emergence of the cT phase at $P > P_{cT}$.

A decrease in the Cr–As distance as a function of P up to P_{cT} is also observed, although at a much smaller rate compared with the evolution of $d_{As–As}$. Above P_{cT}, the compression is stabilized as inferred from the simulation data, which show a decrease of about 5% in total. Meanwhile, the $d_{Cr–Cr}$ interatomic distance decreases with applied pressure from 2.78 to 2.66 Å and then from P_{cT} increases up to ~ 2.72 Å. Finally, the angles As–Cr–As can occur with Cr linking the As ions in the same or adjacent planes. They are labeled as angles α and β, respectively [see Fig. 3(a)]. While these quantities obtained from the simulations tend to
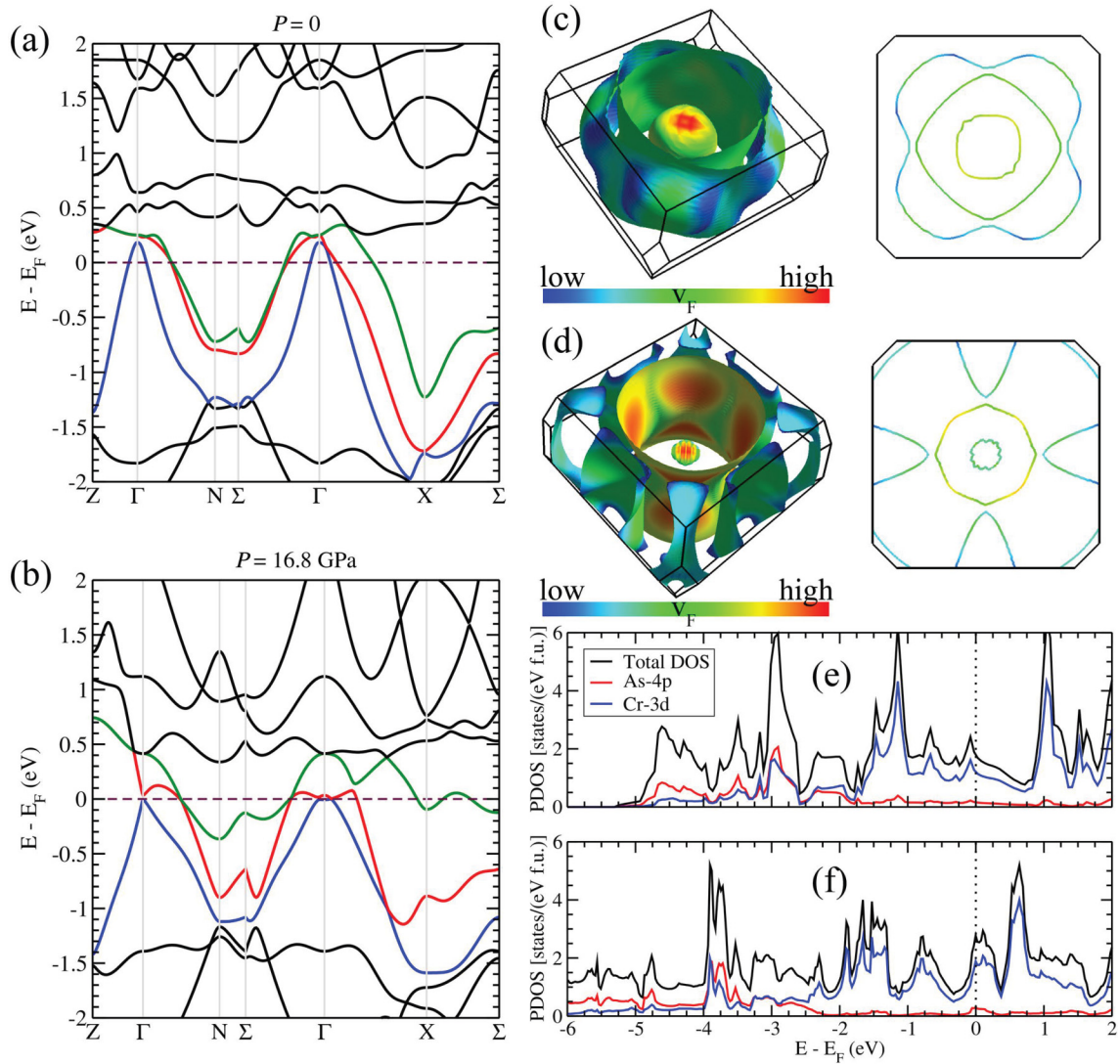
FIG. 5. $SrCr_2As_2$ band structure (a) for equilibrium system at $P = 0$ and (b) for the system compressed at $P = 16.8$ GPa. Fermi surfaces are shown at (c) $P = 0$ and (d) $P = 16.8$ GPa, for the bands represented by blue, red and green curves in (a) and (b). The color scale in (c) and (d) represents the magnitude of the Fermi velocity $\mathbf{v}_F$. Degenerate spin-up and spin-down projected density of states (PDOS) at (e) $P = 0$ and (f) $P = 16.8$ GPa.

a common value at very high pressures as shown in Fig. 4(d), a different behavior was reported for the isostructural compound $BaFe_2As_2$, which starts from common angles around $109°$ which becomes separated above 10 GPa [29] at room temperature. Nonetheless, studies on Fe-based thin films show that superconductivity is induced when such angles approach the regular tetrahedron value [47].

Further insights into the $SrCr_2As_2$ electronic and magnetic properties were also obtained through first-principles simulations. For the magnetic configuration, we have considered the experimentally-observed G-type antiferromagnetic (AFM) order between the Cr atoms [35,36]. The AFM phase is energetically more favorable than the ferromagnetic (FM) phase by 0.35 eV, and by 0.61 eV when compared with the nonmagnetic (NM) phase, as presented in Fig. 4(f). The AFM phase remains the most stable throughout the applied pressure range, although the energy difference $E_{AFM} - E_{FM}$ steadily decreases from the equilibrium system to P_{cT}, becoming 25%

smaller at that point. Beyond P_{cT} the difference decreases even more, and becomes approximately constant around an energy difference of 0.1 eV. On the other hand, $E_{AFM} - E_{NM}$ steadily decreases up to P_{cT} (by 41%), and from that point the energy difference becomes constant at $\sim$0.2 eV. For the equilibrium system, we find a magnetic moment of $2.49\ \mu_B$/Cr atom, which is larger than the experimental value of $1.9\ \mu_B$/Cr atom but in agreement with other DFT simulations [48,49]. In Fig. 4(e) the Cr magnetic moment μ is plotted as a function of P. We observe that initially μ decreases as P increases, and upon the structural phase transition it has a larger decrease; beyond that point the magnetization shows only a small increase, remaining nearly constant around $1.8\ \mu_B$/Cr atom at higher pressure values.

The electronic band structures for $P = 0$ and $P = 16.8$ GPa captured from the DFT simulations are presented in Figs. 5(a) and 5(b), respectively, along the highly symmetric BZ lines presented in Fig. 3(b). For the equilibrium geometry at $P = 0$

[Fig. 5(a)] we observe three holelike Fermi-level crossing bands, which are mostly composed by Cr-$3d_{xy/xz}$ and Cr-$3d_{x^2-y^2}$ orbitals, as shown in Fig. S5 of the SM [42]. In Fig. S5 we can also observe that the As-$4p$ states are mostly localized in the region below -2 eV relative to E_F, which is also captured in the As-$4p$ projected density of states (PDOS) plot presented in Fig. 5(e). Moreover, in Fig. 5(a) there is one crossing band in the $Z\Gamma - N$ direction with a maximum at Γ (blue), whereas three crossing bands in the $\Sigma\Gamma - X$ direction present two maxima (blue and red) and a local minimum (green) at Γ, all above E_F. Above P_{cT} [Fig. 5(b)], two bands (blue and red) lower their energy towards E_F, while the third band (green) is pushed to higher energies. The band structure along $Z\Gamma - N$ presents a maximum and a minimum, which touch each other at the Fermi level. The band with maximum (minimum) along this symmetric path presents a minimum (maximum) band along $\Sigma\Gamma - X$, creating two saddle-point-type Van Hove singularities. It is worth noting that this structure would, in principle, increase the density of states (DOS) available at the Fermi level. Additionally, the presence of electron pockets above P_{cT} can be suggested by the observation of a small parabolic band with a minimum around $\Gamma - X\Sigma$ and a larger near-parabolic band around $X - \Sigma\Gamma$, both in close proximity to the Fermi level.

In Fig. 5(c) we present the Fermi surface (FS) for the equilibrium system. In Fig. 5(c), a small cushion-type hole pocket is formed around the Γ point, and one cylindrical hole pocket is extended around the entire $\Gamma - Z$ axis. The third structure is a corrugated hole pocket around the $\Gamma - Z$ axis, although less extended in this direction, with higher $\mathbf{v}_F$ magnitude concentrated along the ΓX direction. In the Fermi surface above P_{cT} shown in Fig. 5(d), the dimensions of the cushion and cylindrical pockets are reduced around the Γ point. A clear increase in the magnitude of $\mathbf{v}_F$ is observed with a periodic distribution along the surface of the cylindrical pocket. The most significant change occurs for the corrugated pocket, which develops into localized pockets in the boundary of the BZ. If the center of the presented BZ in Fig. 5(d) is translated to the Σ and X points, corrugated cylindrical pockets and four-leaf-clover-type pockets are formed. Remarkably, such a topological change in the Fermi surface at the collapsed phase might be attributed to a Lifshitz transition that allows for the presence of electron pockets around symmetric points of the BZ boundary.

More insights can be gained from the PDOS around the Fermi energy for $P = 0$ [Fig. 5(e)] and $P = 16.8$ GPa [Fig. 5(f)]. For the equilibrium system, we observe that above -2 eV, most of the DOS contribution comes from Cr-$3d$ states. Between -4 and -2 eV there is a hybridization of Cr-$3d$ and As-$4p$ states; below -4 eV the contribution of the As-$4p$ states increases compared with that of the Cr-$3d$ states. Above P_{cT}, the two peaks in Fig. 5(f) around -1.25 and -3 eV are broadened and extended to lower energies. Beyond E_F we observe a sharp peak in Fig. 5(e) at 1.0 eV, coming mostly from Cr-$3d$ states, which above P_{cT} is displaced to 0.5 eV in Fig. 5(f) with a reduced intensity. Most remarkable is the huge increase ($\sim$50%) of the DOS around the Fermi level, which is consistent with the formation of Van Hove singularities predicted by the band structure. In Figs. S5 and S6 of the SM [42] we project all the As-$4p$ and Cr-$3d$ orbitals on the band structure. Above P_{cT}, the intensities of the orbitals with projections along the z direction of the unit cell are enhanced compared with the orbital occupation in the xy plane. This observation also supports the idea of the formation of an interlayer As–As bond in SrCr$_2$As$_2$ in the collapsed phase.

IV. DISCUSSION

A simple model describing the formation of an As–As covalent bond in the c direction in systems similar to SrCr$_2$As$_2$ takes into account the packing of Cr$_2$As$_2^{2-}$ layers. This packing develops a density of states composed by bonding As-$4p$ and Cr-$3d$ orbitals and antibonding As-$4p$ orbitals as the energy is increased [46,50]. As the distance between As and As decreases to the covalent value, a shift in the Fermi level should occur, emptying the antibonding states, which allows for the chemical bond and, as a consequence, the collapsed phase. The interaction between Cr$_2$As$_2^{2-}$ layers together with the presence of the cation Sr^{2+} increases the bare As–As covalent length by 0.5 Å, which explains the occurrence of the collapse around 3 Å in Fig. 4(a). From another point of view, a maximization in the DOS at the Fermi energy associated with a higher degree of Cr-As hybridization would imply an electronically-driven lattice instability [34]. In fact, there is a maximization of the DOS in SrCr$_2$As$_2$ due to Cr-As hybridization observed in Fig. 5(f). Another point to be noted is the predominance of orbitals with z component (Cr and As) above P_{cT} (Figs. S5 and S6 in the SM [42]).

A suppression of the magnetism of SrCr$_2$As$_2$ up to P_{cT} is captured from our DFT results for both local and global scenarios. In the first picture, there is agreement between the decreasing of the Cr magnetic moment and the reduction in $d_{Cr–As}$, which is an additional probe of local magnetic moment as discussed in Refs. [51,52] for BaFe$_2$As$_2$. In comparison, the compression rate of the Cr–As distance is around 0.006 Å/GPa below P_{cT}, which is smaller than the compression rate observed for the Fe–As distance in BaFe$_2$As$_2$ [52]. In fact, a slight magnetostriction effect at the Cr site was observed in SrCr$_2$As$_2$ through a magneto-Raman experiment [53]. From a global point of view, the suppression is characterized by the reduction in the absolute value of the difference $E_{AFM} - E_{NM}$. Above P_{cT} there is a residual Cr magnetic moment and a finite difference $E_{AFM} - E_{NM}$. In this case, spin fluctuations could be one mechanism for magnetism suppression, which would open room for the development of superconductivity.

It can be noticed that above P_{cT} the Fermi surface of SrCr$_2$As$_2$ in Fig. 5(d) assumes a similar shape to that found in other pnictides [54] with the formation of pockets around the boundaries of the BZ. An inspection of the band structure above the transition suggest that these new localized Fermi surfaces are electron pockets. As a consequence, there are possible paths for nesting between hole and electron pockets within the BZ in the collapsed phase of SrCr$_2$As$_2$. Although superconductivity has not been observed in SrCr$_2$As$_2$, its structure (collapsed-tetragonal phase and regular tetrahedron angles), FS topology, and DOS in the cT phase would allow superconductivity if magnetism were completely suppressed. Such suppression could occur in the presence of spin fluctuations or higher applied pressure as indicated in Ref. [34].

V. CONCLUSION

In this paper we address the structural, electronic, and magnetic properties of $SrCr_2As_2$ under high pressures through a combined analysis of synchrotron x-ray diffraction and simulations employing density functional theory. From this approach, bond distances, angles between bonds, the magnetization (2.49 μ_B/Cr atom), and the most stable magnetic phase (AFM) were determined. The Cr magnetic moment and the magnetic energy of the system are suppressed up to P_{cT} and remain essentially constant above this transition. The signatures in the lattice parameters and band structure as a function of pressure suggest an electronically-driven tetragonal to collapsed-tetragonal transition in a $SrCr_2As_2$ polycrystalline sample. Most noteworthy is the emergence of electron pockets at the edges of the Brillouin zone, which creates opportunities for the emergence of superconductivity, possibly following the suppression of magnetism.

[1] Y. Kamihara, T. Watanabe, M. Hirano, and H. Hosono, Iron-based layered superconductor La[O$_{1−x}$F$_x$]FeAs ($x =$ 0.05−0.12) with T_c = 26 K, J. Am. Chem. Soc. **130**, 3296 (2008).

[2] A. Leithe-Jasper, W. Schnelle, C. Geibel, and H. Rosner, Superconducting state in SrFe$_{2−x}$Co$_x$As$_2$ by internal doping of the iron arsenide layers, Phys. Rev. Lett. **101**, 207004 (2008).

[3] A. S. Sefat, R. Jin, M. A. McGuire, B. C. Sales, D. J. Singh, and D. Mandrus, Superconductivity at 22 K in Co-doped BaFe$_2$As$_2$ crystals, Phys. Rev. Lett. **101**, 117004 (2008).

[4] L. Harnagea, S. Singh, G. Friemel, N. Leps, D. Bombor, M. Abdel-Hafiez, A. U. B. Wolter, C. Hess, R. Klingeler, G. Behr, S. Wurmehl, and B. Büchner, Phase diagram of the iron arsenide superconductors Ca(Fe$_{1−x}$Co$_x$)$_2$As$_2$ ($0 \leqslant x \leqslant$ 0.1), Phys. Rev. B **83**, 094523 (2011).

[5] S. Aswartham, M. Abdel-Hafiez, D. Bombor, M. Kumar, A. U. B. Wolter, C. Hess, D. V. Evtushinsky, V. B. Zabolotnyy, A. A. Kordyuk, T. K. Kim, S. V. Borisenko, G. Behr, B. Büchner, and S. Wurmehl, Hole doping in BaFe$_2$As$_2$: The case of Ba$_{1−x}$Na$_x$Fe$_2$As$_2$ single crystals, Phys. Rev. B **85**, 224520 (2012).

[6] N. H. Lee, S.-G. Jung, D. H. Kim, and W. N. Kang, Potassium-doped BaFe$_2$As$_2$ superconducting thin films with a transition temperature of 40 K, Appl. Phys. Lett. **96**, 202505 (2010).

[7] P. L. Alireza, Y. C. Ko, J. Gillett, C. M. Petrone, J. M. Cole, G. G. Lonzarich, and S. E. Sebastian, Superconductivity up to 29 K in SrFe$_2$As$_2$ and BaFe$_2$As$_2$ at high pressures, J. Phys.: Condens. Matter **21**, 012208 (2009).

[8] M. S. Torikachvili, S. L. Bud'ko, N. Ni, and P. C. Canfield, Pressure induced superconductivity in CaFe$_2$As$_2$, Phys. Rev. Lett. **101**, 057006 (2008).

[9] T. Park, E. Park, H. Lee, T. Klimczuk, E. Bauer, F. Ronning, and J. D. Thompson, Pressure-induced superconductivity in CaFe$_2$As$_2$, J. Phys.: Condens. Matter **20**, 322204 (2008).

[10] A. Satya, A. Mani, A. Arulraj, N. C. Shekar, K. Vinod, C. Sundar, and A. Bharathi, Pressure-induced metallization of BaMn$_2$As$_2$, Phys. Rev. B **84**, 180515(R) (2011).

[11] K. A. Filsinger, W. Schnelle, P. Adler, G. H. Fecher, M. Reehuis, A. Hoser, J.-U. Hoffmann, P. Werner, M. Greenblatt, and C. Felser, Antiferromagnetic structure and electronic properties of BaCr$_2$As$_2$ and BaCrFeAs$_2$, Phys. Rev. B **95**, 184414 (2017).

[12] Y. Gallais, R. Fernandes, I. Paul, L. Chauviere, Y.-X. Yang, M.-A. Méasson, M. Cazayous, A. Sacuto, D. Colson, and A. Forget, Observation of incipient charge nematicity in Ba(Fe$_{1−x}$Co$_x$)$_2$As$_2$, Phys. Rev. Lett. **111**, 267001 (2013).

[13] Y. Gallais and I. Paul, Charge nematicity and electronic Raman scattering in iron-based superconductors, Compt. Rend. Phys. **17**, 113 (2016).

[14] W.-L. Zhang, Z. Yin, A. Ignatov, Z. Bukowski, J. Karpinski, A. S. Sefat, H. Ding, P. Richard, and G. Blumberg, Raman scattering study of spin-density-wave-induced anisotropic electronic properties in AFe$_2$As$_2$ (A = Ca, Eu), Phys. Rev. B **93**, 205106 (2016).

[15] P. Massat, D. Farina, I. Paul, S. Karlsson, P. Strobel, P. Toulemonde, M.-A. Méasson, M. Cazayous, A. Sacuto, S. Kasahara, T. Shibauchi, and Y. Matsuda, and Y. Gallais, Charge-induced nematicity in FeSe, Proc. Natl. Acad. Sci. USA **113**, 9177 (2016).

[16] H. Yamase and R. Zeyher, Electronic Raman scattering from orbital nematic fluctuations, Phys. Rev. B **88**, 125120 (2013).

[17] U. F. Kaneko, P. Gomes, A. Garcia-Flores, J.-Q. Yan, T. A. Lograsso, G. Barberis, D. Vaknin, and E. Granado, Nematic fluctuations and phase transitions in LaFeAsO: A Raman scattering study, Phys. Rev. B **96**, 014506 (2017).

[18] U. F. Kaneko, M. Piva, C. Jesus, M. Saleta, R. Urbano, P. Pagliuso, and E. Granado, Evidence of precursor orthorhombic domains well above the electronic nematic transition temperature in Sr(Fe$_{1−x}$Co$_x$)$_2$As$_2$, J. Phys.: Condens. Matter **31**, 495402 (2019).

[19] T. Böhm, R. Hosseinian Ahangharnejhad, D. Jost, A. Baum, B. Muschler, F. Kretzschmar, P. Adelmann, T. Wolf, H.-H. Wen, and J.-H. Chu, Superconductivity and fluctuations in Ba$_{1−p}$K$_p$Fe$_2$As$_2$ and Ba(Fe$_{1−n}$Co$_n$)$_2$As$_2$, Phys. Stat. Sol. B **254**, 1600308 (2017).

[20] U. Karahasanovic, F. Kretzschmar, T. Böhm, R. Hackl, I. Paul, Y. Gallais, and J. Schmalian, Manifestation of nematic degrees of freedom in the Raman response function of iron pnictides, Phys. Rev. B **92**, 075134 (2015).

[21] M. Khodas and A. Levchenko, Raman scattering as a probe of nematic correlations, Phys. Rev. B **91**, 235119 (2015).

[22] H. Yamase and R. Zeyher, Spin nematic fluctuations near a spin-density-wave phase, New J. Phys. **17**, 073030 (2015).

[23] F. Kretzschmar, T. Böhm, U. Karahasanovic, B. Muschler, A. Baum, D. Jost, J. Schmalian, S. Caprara, M. Grilli, C. Di Castro, J. G. Analytis, J.-H. Chu, I. R. Fisher, and R. Hackl, Critical spin fluctuations and the origin of nematic order in Ba(Fe$_{1-x}$Co$_x$)$_2$As$_2$, Nat. Phys. **12**, 560 (2016).

[24] W. O. Uhoya, G. M. Tsoi, Y. K. Vohra, M. A. McGuire, and A. S. Sefat, Structural phase transitions in EuFe$_2$As$_2$ superconductor at low temperatures and high pressures, J. Phys.: Condens. Matter **23**, 365703 (2011).

[25] W. Uhoya, A. Stemshorn, G. Tsoi, Y. K. Vohra, A. S. Sefat, B. C. Sales, K. M. Hope, and S. T. Weir, Collapsed tetragonal phase and superconductivity of BaFe$_2$As$_2$ under high pressure, Phys. Rev. B **82**, 144118 (2010).

[26] A. Kreyssig, M. A. Green, Y. Lee, G. D. Samolyuk, P. Zajdel, J. W. Lynn, S. L. Bud'ko, M. S. Torikachvili, N. Ni, S. Nandi, J. B. Leão, S. J. Poulton, D. N. Argyriou, B. N. Harmon, R. J. McQueeney, P. C. Canfield, and A. I. Goldman, Pressure-induced volume-collapsed tetragonal phase of CaFe$_2$As$_2$ as seen via neutron scattering, Phys. Rev. B **78**, 184517 (2008).

[27] A. I. Goldman, A. Kreyssig, K. Prokeš, D. K. Pratt, D. N. Argyriou, J. W. Lynn, S. Nandi, S. A. J. Kimber, Y. Chen, Y. B. Lee, G. Samolyuk, J. B. Leão, S. J. Poulton, S. L. Bud'ko, N. Ni, P. C. Canfield, B. N. Harmon, and R. J. McQueeney, Lattice collapse and quenching of magnetism in CaFe$_2$As$_2$ under pressure: A single-crystal neutron and X-ray diffraction investigation, Phys. Rev. B **79**, 024513 (2009).

[28] J. H. Soh, G. S. Tucker, D. K. Pratt, D. L. Abernathy, M. B. Stone, S. Ran, S. L. Bud'ko, P. C. Canfield, A. Kreyssig, R. J. McQueeney, and A. I. Goldman, Inelastic neutron scattering study of a nonmagnetic collapsed tetragonal phase in nonsuperconducting CaFe$_2$As$_2$: Evidence of the impact of spin fluctuations on superconductivity in the iron-arsenide compounds, Phys. Rev. Lett. **111**, 227002 (2013).

[29] R. Mittal, S. K. Mishra, S. L. Chaplot, S. V. Ovsyannikov, E. Greenberg, D. M. Trots, L. Dubrovinsky, Y. Su, Th. Brueckel, S. Matsuishi, H. Hosono, and G. Garbarino, Ambient- and low-temperature synchrotron x-ray diffraction study of BaFe$_2$As$_2$ and CaFe$_2$As$_2$ at high pressures up to 56 GPa, Phys. Rev. B **83**, 054503 (2011).

[30] J.-J. Ying, L.-Y. Tang, V. V. Struzhkin, H.-K. Mao, A. G. Gavriliuk, A.-F. Wang, X.-H. Chen, and X.-J. Chen, Tripling the critical temperature of KFe$_2$As$_2$ by carrier switch, arXiv:1501.00330.

[31] D. Guterding, S. Backes, H. O. Jeschke, and R. Valentí, Origin of the superconducting state in the collapsed tetragonal phase of KFe$_2$As$_2$, Phys. Rev. B **91**, 140503(R) (2015).

[32] S. V. Borisenko, V. B. Zabolotnyy, D. V. Evtushinsky, T. K. Kim, I. V. Morozov, A. N. Yaresko, A. A. Kordyuk, G. Behr, A. Vasiliev, R. Follath, and B. Büchner, Superconductivity without nesting in LiFeAs, Phys. Rev. Lett. **105**, 067002 (2010).

[33] W. T. Jayasekara, U. S. Kaluarachchi, B. G. Ueland, A. Pandey, Y. B. Lee, V. Taufour, A. Sapkota, K. Kothapalli, N. S. Sangeetha, G. Fabbris, L. S. I. Veiga, Y. Feng, A. M. dos Santos, S. L. Bud'ko, B. N. Harmon, P. C. Canfield, D. C. Johnston, A. Kreyssig, and A. I. Goldman, Pressure-induced collapsed-tetragonal phase in SrCo$_2$As$_2$, Phys. Rev. B **92**, 224103 (2015).

[34] P. G. Naumov, K. Filsinger, O. I. Barkalov, G. H. Fecher, S. A. Medvedev, and C. Felser, Pressure-induced transition to the collapsed tetragonal phase in BaCr$_2$As$_2$, Phys. Rev. B **95**, 144106 (2017).

[35] P. Das, N. S. Sangeetha, G. R. Lindemann, T. Heitmann, A. Kreyssig, A. I. Goldman, R. J. McQueeney, D. C. Johnston, and D. Vaknin, Itinerant G-type antiferromagnetic order in SrCr$_2$As$_2$, Phys. Rev. B **96**, 014411 (2017).

[36] Q.-P. Ding, S. Pakira, N. S. Sangeetha, E. H. Krenkel, E. I. Timmons, M. A. Tanatar, R. Prozorov, D. C. Johnston, and Y. Furukawa, Itinerant G-type antiferromagnet SrCr$_2$As$_2$ studied by magnetization, heat capacity, electrical resistivity, and NMR measurements, Phys. Rev. B **105**, 134408 (2022).

[37] P. Giannozzi, S. Baroni, N. Bonini, M. Calandra, R. Car, C. Cavazzoni, D. Ceresoli, G. L. Chiarotti, M. Cococcioni, I. Dabo, A. Dal Corso, S. de Gironcoli, S. Fabris, G. Fratesi, R. Gebauer, U. Gerstmann, C. Gougoussis, A. Kokalj, M. Lazzeri, L. Martin-Samos *et al.*, QUANTUM ESPRESSO: a modular and open-source software project for quantum simulations of materials, J. Phys.: Condens. Matter **21**, 395502 (2009).

[38] J. P. Perdew, K. Burke, and M. Ernzerhof, Generalized gradient approximation made simple, Phys. Rev. Lett. **77**, 3865 (1996).

[39] G. Kresse and D. Joubert, From ultrasoft pseudopotentials to the projector augmented-wave method, Phys. Rev. B **59**, 1758 (1999).

[40] H. J. Monkhorst and J. D. Pack, Special points for Brillouin-zone integrations, Phys. Rev. B **13**, 5188 (1976).

[41] M. Kawamura, FermiSurfer: Fermi-surface viewer providing multiple representation schemes, Comput. Phys. Commun. **239**, 197 (2019).

[42] See Supplemental Material at http://link.aps.org/supplemental/10.1103/PhysRevB.108.195114 for visualization of 2D raw images of the x-ray diffraction for selected images, the raw intensity vs 2θ diffraction profiles as a function of pressure, and the Le Bail analysis for four of these profiles. The widths obtained from Lorentzian functions of the ruby luminescence as a function of pressure, the second-order Birch-Murnaghan equation, and the orbital-projected electronic states for equilibrium and above the tetragonal to collapsed-tetragonal transition are also shown. References [37,43,55] are also included in the Supplemental Material.

[43] J. P. Poirier, *Introduction to the Physics of the Earth's Interior*, 2nd ed. (Cambridge University Press, Cambridge, 2000), p. 312

[44] Z. Yu, L. Wang, L. Wang, H. Liu, J. Zhao, C. Li, S. Sinogeikin, W. Wu, J. Luo, N. Wang, K. Yang, Y. Zhao, and H. Mao, Conventional empirical law reverses in the phase transitions of 122-type iron-based superconductors, Sci. Rep. **4**, 7172 (2014).

[45] W. Uhoya, J. Montgomery, G. Samudrala, G. Tsoi, Y. Vohra, S. Weir, and A. Sefat, High-pressure structural phase transitions in chromium-doped BaFe$_2$As$_2$, J. Phys.: Conf. Ser. **377**, 012016 (2012).

[46] J. Jeffries, N. Butch, K. Kirshenbaum, S. Saha, G. Samudrala, S. Weir, Y. Vohra, and J. Paglione, Suppression of magnetism and development of superconductivity within the collapsed tetragonal phase of Ca$_{0.67}$Sr$_{0.33}$Fe$_2$As$_2$ under pressure, Phys. Rev. B **85**, 184501 (2012).

[47] J.-H. Kanga, J.-W. Kimb, P. J. Ryanb, L. Xied, L. Guoa, C. Sundahla, J. Schada, N. Campbelle, Y. G. Collantes,

E. E. Hellstromf, M. S. Rzchowskie, and C.-B. Eoma, Superconductivity in undoped BaFe$_2$As$_2$ by tetrahedral geometry design, Proc. Natl. Acad. Sci. U. S. A. **117**, 21170 (2020).

[48] W. Zhou, P. Hu, S. Li, and S. Wu, First-principles study of the magnetic and electronic properties of ACr$_2$As$_2$ (A = Sr, Ba), J. Magn. Magn. Mater. **476**, 254 (2019).

[49] A. Hamri, M. Djermouni, A. Zaoui, and S. Kacimi, *Ab-initio* study of the electronic structure and magnetic properties of ACr$_2$Pn$_2$ (A = Ba, Sr, Ca, Sc, K; Pn = As, P), J. Phys. Chem. Solids **150**, 109850 (2021).

[50] R. Hoffmann and C. Zheng, Making and breaking bonds in the solid state: The ThCr$_2$Si$_2$ structure, J. Phys. Chem. **89**, 4175 (1985).

[51] M. Johannes, I. Mazin, and D. Parker, Effect of doping and pressure on magnetism and lattice structure of iron-based superconductors, Phys. Rev. B **82**, 024527 (2010).

[52] E. Granado, L. Mendonça-Ferreira, F. Garcia, G. de M. Azevedo, G. Fabbris, E. M. Bittar, C. Adriano, T. Garitezi, P. Rosa, L. Bufaiçal, M. A. Avila, H. Terashita, and P. G. Pagliuso, Pressure and chemical substitution effects in the local atomic structure of BaFe$_2$As$_2$, Phys. Rev. B **83**, 184508 (2011).

[53] U. F. Kaneko, M. Teodoro, P. Gomes, N. S. Sangeetha, and D. C. Johnston, Electron-phonon coupling enhancement and displacive magnetostructural transition in SrCr$_2$As$_2$ under magneto-Raman spectroscopy, J. Phys.: Condens. Matter **33**, 105401 (2021).

[54] D. C. Johnston, The puzzle of high temperature superconductivity in layered iron pnictides and chalcogenides, Adv. Phys. **59**, 803 (2010).

[55] S. Klotz, J.-C. Chervin, P. Munsch, and G. Le Marchand, Hydrostatic limits of 11 pressure transmitting media, J. Phys. D: Appl. Phys. **42**, 075413 (2009).